Journal of Mathematical Imaging and Vision 19: 199–218, 2003

Level Set Curve Matching and Particle Image Velocimetry for Resolving Chemistry and Turbulence Interactions in Propagating Flames

RAFEEF ABU-GHARBIEH
Department of Electrical and Computer Engineering, Ryerson University, Toronto, ON M5B 2K3, Canada; Department of Signals and Systems, Chalmers University of Technology, Göteborg 412 96, Sweden
rafeef@ee.ryerson.ca

GHASSAN HAMARNEH AND TOMAS GUSTAVSSON
Department of Signals and Systems, Chalmers University of Technology, Göteborg 412 96, Sweden

CLEMENS KAMINSKI
Department of Chemical Engineering, Cambridge University, Cambridge CB2 3RA, UK

Abstract. We present an imaging, image processing, and image analysis framework for facilitating the separation of flow and chemistry effects on local flame front structures. Image data of combustion processes are obtained by a novel technique that combines simultaneous measurements of distribution evolutions of OH radicals and of instantaneous velocity fields in turbulent flames. High-speed planar laser induced fluorescence (PLIF) of OH radicals is used to track the response of the flame front to the turbulent flow field. Instantaneous velocity field measurements are simultaneously performed using particle image velocimetry (PIV). Image analysis methods are developed to process the experimentally captured data for the quantitative study of turbulence/chemistry interactions. The flame image sequences are smoothed using nonlinear diffusion filtering and flame boundary contours are automatically segmented using active contour models. OH image sequences are analyzed using a curve matching algorithm that incorporates level sets and geodesic path computation to track the propagation of curves representing successive flame contours within a sequence. This makes it possible to calculate local flame front velocities, which are strongly affected by turbulence/chemistry interactions. Since the PIV data resolves the turbulent flow field, the combined technique allows a more detailed investigation of turbulent flame phenomena.

Keywords: image analysis, image processing, tracking, contour matching, curve matching, level sets, geodesic paths, non-linear diffusion, segmentation, active contour models, Snakes, PLIF, PIV, time-resolved imaging, turbulence, chemistry interactions

1. Introduction

Understanding the stability of turbulent non-premixed flames is both of fundamental and practical importance because of their widespread appearance in technical applications. To increase the understanding of turbulence and chemistry interaction phenomena such as local flame extinction, flame stabilization and liftoff, experimental studies have to be performed in well-characterized turbulent flames. Local flame instabilities are always the consequence of an interaction between fluid motion and flame chemistry and their understanding has far reaching implications in the design of next generation technical combustion devices, such as aero engines and low pollution gas turbines. In the past, turbulent combustion research has mostly focused on the measurement of temporally uncorrelated events. Such data can be used for the construction of PDFs

(probability density functions) and comparisons with RANS (Reynold averaged Navier Stokes) modeling approaches. However, since turbulence is inherently a time-dependent phenomenon, model construction will ultimately benefit from the provision of time correlated measurement data. Very few experiments have been done in this respect, owing to the extreme complexity of the measurements and subsequent data evaluation. Point measurements of time correlated quantities in turbulent flames have recently been reported by Renfro et al. [26] using an 80 MHz repetition rate Ti:Sapphire laser system. Double pulse line images of majority species and temperature in turbulent jet flames have been recorded by Brockhinke et al. [5]. Two dimensional double pulse imaging techniques have also been employed, for example, to measure the temporal development of OH concentration fields from which turbulent fluctuation time scales could be measured [3, 12]. Longer sequence recordings of turbulent reactive flow structures have been reported by Winter and Long using Mie scattering of aerosols seeded into the fuel [30]. Similarly OH and O_2 were imaged at low repetition frequencies (250 Hz) by Kychakoff et al. [21]. High quality high repetition rate planar laser induced fluorescence (PLIF) image sequences of flame-produced radicals can nowadays be recorded at repetition rates exceeding tens of kHz [11, 17]. Combination of PLIF and particle image velocimetry (PIV) measurements that were simultaneously performed on a single shot basis has also been demonstrated [13, 28].

This paper presents a novel technique that combines simultaneous measurements of OH radical distributions and of instantaneous velocity fields in turbulent flames. High speed PLIF of OH is used to track the response of flame fronts to turbulent flow fields. Instantaneous velocity field measurements are simultaneously performed using PIV where small particles are seeded in fluid flows in order to trace their motion. Measurements of both velocity and species concentrations (captured at the same time) allow detailed studies of the interaction between flow and chemistry in turbulent flames.

The resulting experimental image data create large demands on data reduction, image processing and image analysis techniques. A number of image processing techniques have been reported in the literature for studying structures and velocities in flame images obtained by PLIF. Widely used tools for segmenting flame fronts include simple and adaptive thresholding. One way for setting the threshold values is to study the image intensity histograms [27]. However, these simple approaches do not work well in complex cases often resulting in loss of details or appearance of discontinuities (holes) in the segmented structures. Other approaches include using spatial image gradients rather than intensities for setting the threshold values [20]. Nonetheless this still suffers from the problems of determining the correct thresholds and usually result in contour gaps and noise falsely detected as signal. Other techniques used for studying the properties of flame contours or surfaces include deploying fractal geometry concepts for describing wrinkled flame fronts [7, 15]. These methods have been used to provide estimates of turbulent flame velocities [14] nevertheless they introduce difficulties including the determination of correct fractal parameters such as the fractal dimension.

This paper focuses on computational methods for extracting flame front velocities from our experimentally captured OH-PLIF data and quantitatively comparing them with flow field velocities extracted from the PIV measurements. The techniques can be used to study the dynamics of turbulence and chemistry interactions in real time. OH image sequences are analyzed to extract the flame front velocity, which is a function of both global flow and chemistry effects. The flame images are first smoothed using non-linear diffusion filtering for enhancement and noise reduction. They are then segmented using active contour models (snakes) and their resulting boundary curves subsequently matched in order to reconstruct the flame's motion between successive experimental frames and to estimate flame front velocities. In [1] we propose an approach for flame front velocity estimation employing a frequency-domain interpolation scheme. Here, we propose a more sophisticated technique where velocities are estimated through a curve matching procedure based on the calculation of geodesic paths between curves that are level set representations of flame boundaries. This enables successful handling of sharp edges, cusps, as well as topological changes in flame structure which were previously difficult to accomplish. Lastly, the flow velocities obtained through simultaneous PIV measurements are subtracted from the flame front velocities thus allowing for chemical timescales to be isolated.

2. Experimental Aspects

A schematic diagram illustrating the experimental set-up for the simultaneous OH-PLIF and PIV

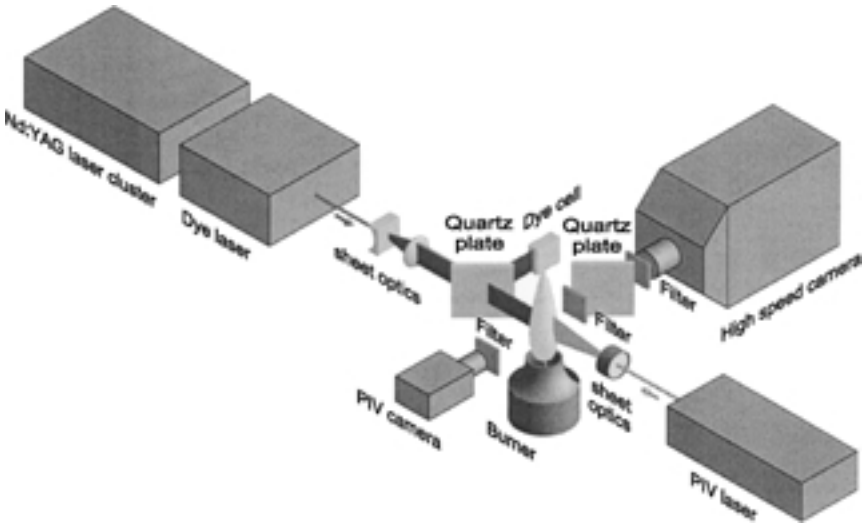

Figure 1. Experimental set-up used for simultaneous measurements of time-resolved OH concentrations and flow fields. The OH-PLIF system is shown to the upper left and the PIV system is shown to the lower right.

measurements is shown in Fig. 1. The flames imaged in this study are non-premixed flames stabilized on a co-flow burner that consists of an 8 mm inner diameter tube with a thinned rim at the exit, surrounded by a concentric contoured nozzle with an inner diameter of 140 mm. A mixture of H_2 (33.2% by volume), CH_4 (22.1%), and N_2 (44.7%) is used as fuel. The exit velocity of the fuel jet is 55 m/s, corresponding to a Reynolds number of around 20,000. The surrounding co-flow of air has an exit velocity of 0.3 m/s. Both fuel flow and co-flow are seeded with 1 μm titanium (TiO_2) particles. The OH-PLIF signal is detected at right angles using a high-speed camera. A cell filled with fluorescing dye solution is used to perform online beam profile measurements. This makes the beam profile information available simultaneously with the OH-PLIF image for subsequent compensation for laser profile fluctuations. A cylindrical lens telescope is used to create the PIV laser sheet and to direct it into the flame. The PIV camera is positioned in a direction normal to the laser sheets, and on the opposite side of the burner to the PLIF camera. Details on the experimental setup and the obtained measurements are reported in [16]. A brief description of the imaging procedures is given in the following two sections.

2.1. OH-PLIF Measurements

The OH-PLIF image data sequences are obtained using a high-speed laser and detector system described in detail in [10, 11, 17]. The principle of PLIF is to form a light sheet that traverses the flame from a laser beam using suitable optics. When the wavelength is tuned to match a molecular resonance line of OH then light from the sheet is inelastically scattered from the OH radicals present in the interaction region. This scattered light is detected using CCD camera arrangements. The laser pump source is an Nd:YAG laser cluster consisting of four individual laser heads. By firing the individual lasers in series a very fast burst of four laser pulses could be obtained with time separations varying from $\sim$5 ns up to 100 ms between consecutive pulses. The pulse train from the Nd:YAG laser cluster pumps a commercial tunable dye laser operating on Rhodamine 590 dye the output of which was frequency doubled to obtain radiation in the wavelength region where OH absorbs. The PLIF detector is a high-speed framing camera consisting of eight individual CCD cameras. Signals are collected via a common optical input and split into eight identical copies, which are relayed to the individual cameras (only 4 were used in the present study). By using short exposure times and by exposing the eight cameras in series, an image sequence could be captured with an interframe time resolution as low as 10 ns (theoretically possible although in practice this is not needed for technical flows). Example sequences of the captured images are shown in Fig. 2 (premixed flame) and Fig. 3 (diffusion flame). The local intensities in the recorded image sequences are a function of the local OH concentration in the flame. Since OH is

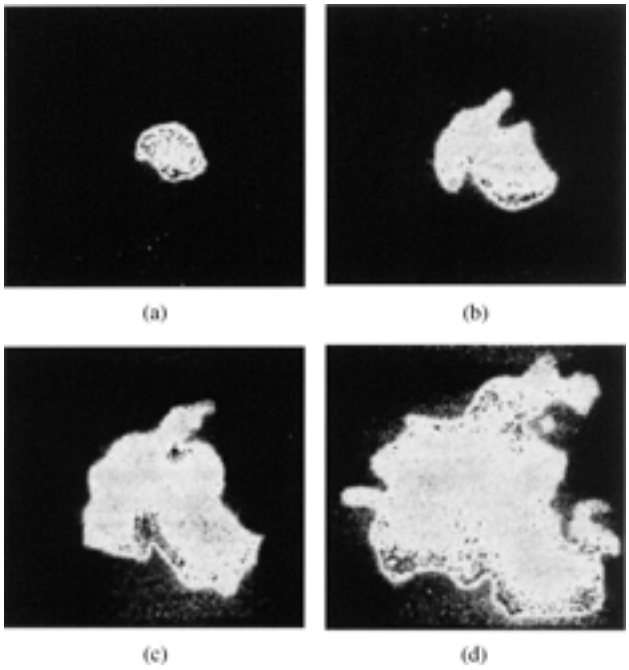

Figure 2. A premixed flame sequence. (a)–(d) Four frames captured with 1.7 millisecond interframe interval.

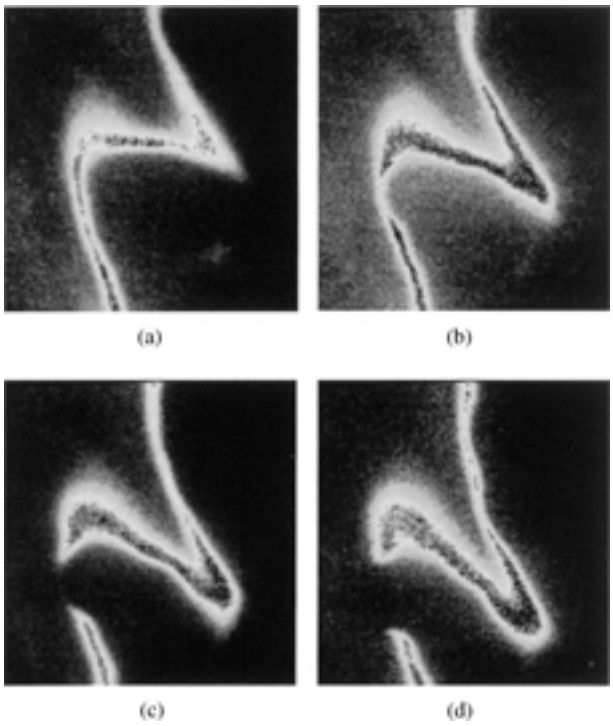

Figure 3. A diffusion flame sequence. (a)–(d) Four frames captured with 125 microsecond inter-frame interval.

formed in the reaction zone of the flame and is rapidly quenched by cold unreacted gases, it is a good indicator of the flame front position where the reaction zone is thin. In hot combusted gases, OH is removed more slowly, and a certain equilibrium concentration prevails depending on local temperatures and burnt gas composition.

2.2. *PIV Measurements*

Light from two Nd:YAG lasers is combined and frequency-doubled to generate two green light pulses. Mie scattering signals from seeded TiO_2 particles are detected using a CCD camera. The scattered light is registered as two individual images by the single CCD camera, which is of frame transfer type. The 2-D flow field could be deduced from each pair of PIV images by applying a cross correlation technique using the Dantec PIV2000 processor and Dantec FlowManager software. More details on this are reported in [16].

3. Image Processing and Analysis

3.1. *Non-Linear Diffusion Filtering*

To improve signal to noise ratios in OH-PLIF image sequences the images are smoothed using non-linear diffusion filtering or edge preserving filtering. The method is based on the original approach formulated by Perona and Malik [25]. The principle is to smooth out noise locally by diffusive flow while at the same time prevent flow across object boundaries. By a proper choice of the diffusion kernel, object boundaries may be enhanced and physical gradients sharpened hence simplifying subsequent localization of object boundaries.

Diffusion can be thought of as the physical process that equilibrates concentration differences without creating or destroying mass. Mathematically, this is described by Fick's law

$$j = -D \cdot \nabla I \tag{1}$$

where the flux j is generated to compensate for the concentration gradient ∇I, and D is a tensor that describes the relation between the two [29]. Using the continuity equation (conservation of mass) $\partial_t(I) = -\mathrm{div}(j)$ we get

$$\partial_t(I) = \mathrm{div}(D \cdot \nabla I). \tag{2}$$

However, the solution of the linear diffusion equation with a scalar diffusivity $D = d$, $\partial_t I = \mathrm{div}(d \nabla I)$, turns out to be the same operation as convolving the concentration image I with a Gaussian kernel of width $\sqrt{2t}$. Perona and Malik proposed to exchange the scalar diffusion constant d with a scalar valued function g of the gradient of the gray levels in the image. The diffusion equation then becomes

$$\partial_t I = \mathrm{div}(g(|\nabla I|)\nabla I). \tag{3}$$

The length of the gradient vector $|\nabla I|$ is a good measure of the edge strength of the current location, which is dependent on the differential structure of the image. This dependence makes the diffusion process nonlinear. In our case the imaged data is filtered using the equation

$$\partial_t I = \mathrm{div}(g(|\nabla(G_\sigma * I)|)\nabla I) \tag{4}$$

where I represents the intensity of the image under consideration, and $g(|\nabla(G_\sigma * I)|)$ represents a locally adaptive diffusive strength. The latter is made inversely proportional to the gradient ∇I in the image itself after smoothing with a Gaussian kernel G_σ of width σ, which is done for stability reasons [6]. As a diffusivity function we use

$$g(s) = 1 - \exp\left(\frac{-C_m}{(s/\lambda)^m}\right) \tag{5}$$

where m is a positive integer and $C_m > 0$ is a constant whose value determines the direction of the flux function ($m = 8$ and $C_m = 3.315$ are used here). $\lambda > 0$ acts as a contrast parameter separating regions of forward diffusion from regions of backward diffusion. In practice we achieved good results by setting λ to 70% of the minimum edge strength we wish to preserve and σ within the interval 0.5–1. Full details of the numerical implementations as well as the criteria for parameter selection are described in [22]. Figures 4 and 5 show example results obtained by non-linear smoothing of flame image sequences as described above.

3.2. *Flame Segmentation*

Active contour models (ACM) or snakes [18] are used to segment the flame structures in order to identify flame front boundaries (used as input to the curve matching algorithm as will be described in the next

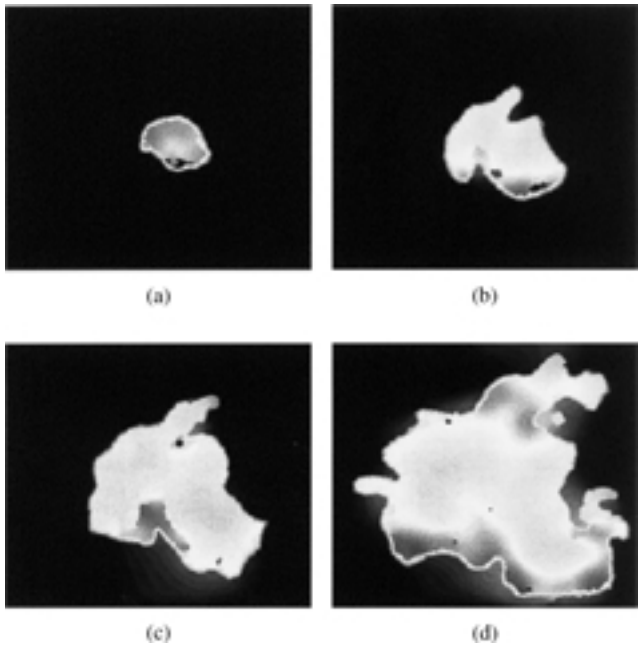

Figure 4. Smoothing the images of Fig. 2 using non-linear diffusion filtering.

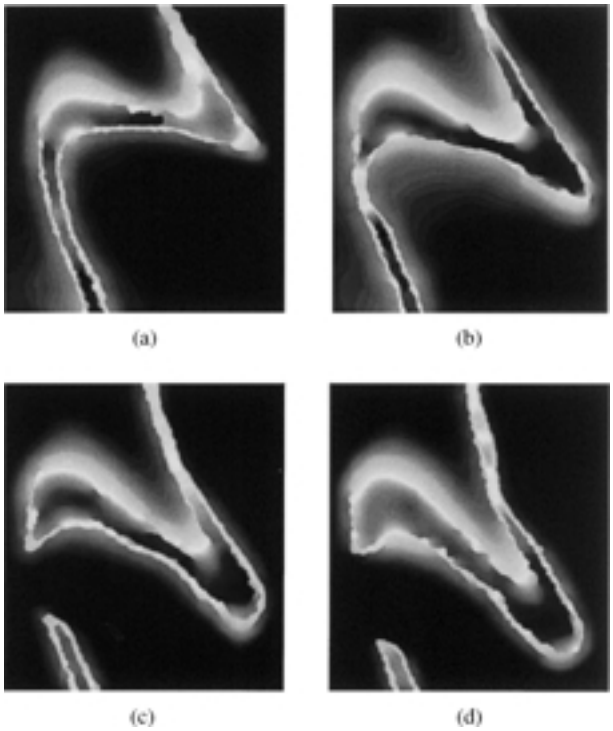

Figure 5. Smoothing the images of Fig. 3 using non-linear diffusion filtering.

section). An initial flame contour is represented by a number of nodes (comprising a snake) and is iteratively deformed by applying different 'forces' on its nodes thus driving the snake towards the object to be segmented. The fundamental equation used to simulate the deformations of the discrete snake contour is

$$\mu\ddot{\mathbf{v}}_i + \gamma\dot{\mathbf{v}}_i + \alpha\mathbf{F}_i^{\text{tensile}} + \beta\mathbf{F}_i^{\text{flexural}} = \mathbf{F}_i^{\text{external}} + \mathbf{F}_i^{\text{inflation}} \tag{6}$$

where $\mathbf{v}_i(t) = (x_i(t), y_i(t))$ are the locations of the snake vertices (i.e. coordinates of nodes). $i = 1, 2, \ldots, N$ where N is the number of nodes, $\dot{\mathbf{v}}$ and $\ddot{\mathbf{v}}$ are the first and second time derivatives of $\mathbf{v}$, μ is the mass, and γ is a damping coefficient. α and β are weighting factors, and $\mathbf{F}_i^{\text{tensile}}$, $\mathbf{F}_i^{\text{flexural}}$, $\mathbf{F}_i^{\text{external}}$, $\mathbf{F}_i^{\text{inflation}}$ are the different forces deforming the snake.

In static image segmentation scenarios the mass μ is often set to zero and a finite difference derivative approximation $\dot{\mathbf{v}}_i = (\mathbf{v}_i(t + \Delta t) - \mathbf{v}_i(t))/\Delta t$ is used where Δt is a finite time step. This yields the following equation for updating the position of any snake node i

$$\mathbf{v}_i(t + \Delta t) = \mathbf{v}_i(t) - \frac{\Delta t}{\gamma}\big(\alpha\mathbf{F}_i^{\text{tensile}}(t) + \beta\mathbf{F}_i^{\text{flexural}}(t) - \mathbf{F}_i^{\text{external}}(t) - \mathbf{F}_i^{\text{inflation}}(t)\big). \tag{7}$$

$\mathbf{F}_i^{\text{tensile}}(t) = 2\mathbf{v}_i(t) - \mathbf{v}_{i-1}(t) - \mathbf{v}_{i+1}(t)$ is the tensile force acting on node i at time t, which resists stretching. $\mathbf{F}_i^{\text{flexural}}(t) = 2\mathbf{F}_i^{\text{tensile}}(t) - \mathbf{F}_{i-1}^{\text{tensile}}(t) - \mathbf{F}_{i+1}^{\text{tensile}}(t)$ is the flexural force, which resists bending. $\mathbf{F}_i^{\text{external}}(t)$ is an external image-derived force that causes the snake nodes to move towards regions of higher intensity gradients in the image and is given by $\mathbf{F}_i^{\text{external}}(t) = \nabla P(x_i(t), y_i(t))$ where $P(x, y) \propto -\|\nabla I_s(x, y)\|$ and $I_s(x, y)$ is the intensity of the pixel (x, y) in a smoothed version of the original image. $\mathbf{F}_i^{\text{inflation}}(t) = F(I_s(x_i, y_i))\,\mathbf{n}_i(t)$ is the inflation force, which enables the initialization of the snake farther away from the target boundary, and $\mathbf{n}_i(t)$ is a unit vector in the direction normal to the contour at node i. The binary function

$$F(I(x, y)) = \begin{cases} +1 & \text{if } I(x, y) \geq T \\ -1 & \text{otherwise} \end{cases} \tag{8}$$

links the inflation force to the image data where T is an image intensity threshold. The values used here are $\alpha = 1$, $\beta = 0.5$, and $T = 80\%$ of the maximum image intensity which are kept the same for all images. Details of the segmentation procedure are reported in [1]. Figure 6 illustrates an example of the progress of snake iterations as it moves towards the flame boundary. More segmentation examples are shown in Figs. 7 and 8.

4. Flame Front Tracking

A contour matching algorithm is employed to track evolving flame fronts extracted from OH-PLIF image datasets. The method is based on the computation of a set of geodesic paths connecting two curves on a cost surface [2]. The curves are implicitly represented using level sets, which facilitates the handling of complex curves especially those with sharp edges and cusps, and also allows for arbitrary topological changes in the curve structure. An additional term is incorporated in the cost function, on which the optimal paths are computed, which steers landmark point pairs with established correspondence to be matched.

4.1. *Locating Optimal Paths*

In [9] it is shown that geodesic paths between a set of source contour points, S, and a set of destination contour points, D, on a surface $Z = (x, y, z(x, y))$, are those that minimize a certain cost function $f(x, y)$ along their path. In order to obtain matching routes between the two curves S and D, this cost function must characterize the similarity between them, and must also enable the matching to be symmetric, i.e. the optimal paths obtained using this function should be the same whether S is matched to D or vice versa. One such function is

$$f(x, y) = D_S + D_D \tag{9}$$

where D_S and D_D are the geodesic distance maps of S and D, respectively. In order to calculate D_S and D_D, the ideas developed by Kimmel et al. are utilized. In [19] it is proven that the evolution of the equal geodesic distance contour of a curve on the surface Z (if restricted to graph surfaces) is given by

$$\vec{\alpha_t}(s, t) = \sqrt{an_1^2 + bn_2^2 - cn_1n_2}\vec{n} \tag{10}$$

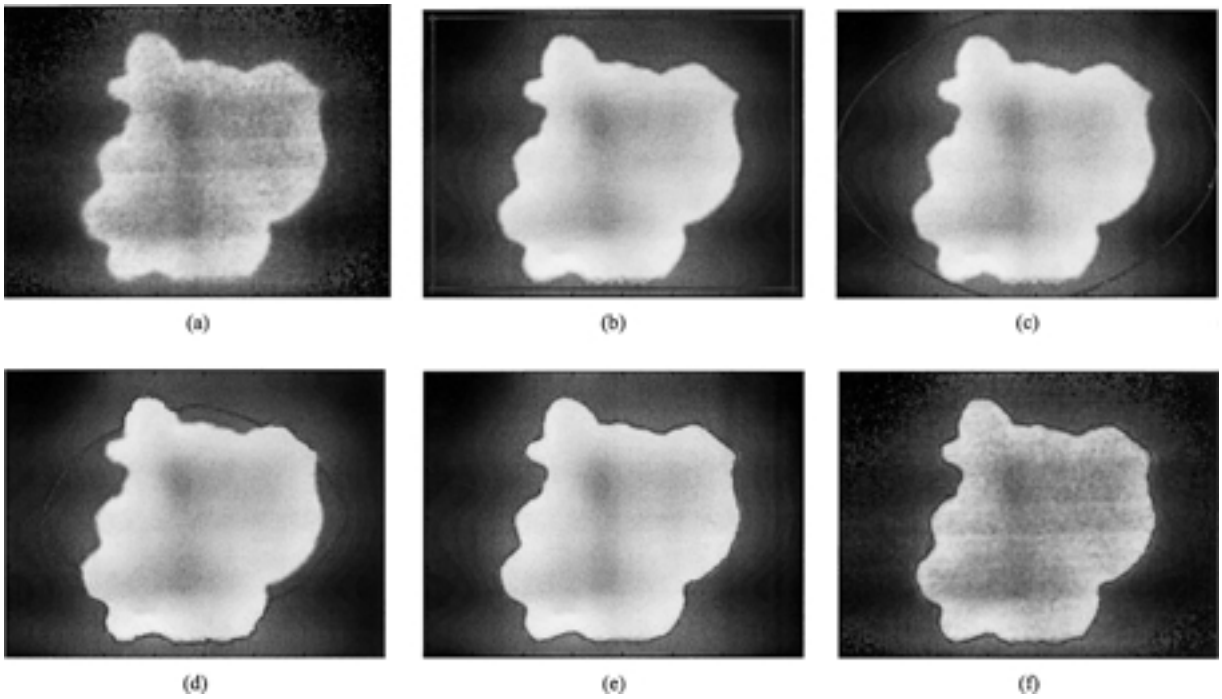

Figure 6. Progress of snake iterations. (a) Original raw image. (b) Initial snake initialized on the non-linearly diffused image. (c)–(e) Snake after 1, 25, and 85 iterations, respectively. (f) Final snake segmentation result overlaid on the original raw image.

where $\vec{n} = (n_1, n_2)$ is the normal to the contour. a, b, and c are coefficients that depend on the gradients of the surface on which the geodesic paths are to be calculated and are given by $a = \frac{1+q^2}{1+p^2+q^2}$, $b = \frac{1+p^2}{1+p^2+q^2}$, and $c = \frac{2pq}{1+p^2+q^2}$, where $p = \frac{\partial z(x,y)}{\partial x}$ and $q = \frac{\partial z(x,y)}{\partial y}$.

4.2. Level Set Representation

In the previous section, it is shown that the evolution of the equal geodesic distance contour depends on the curve's parameterization. Since estimating the normal components using derivatives becomes inaccurate and unstable with complex curves, a non-parametric representation of the curve is needed. By incorporating a level set representation of the curves to be matched, the resulting equivalent evolution equation thus becomes

$$\phi_t = \sqrt{a\phi_x^2 + b\phi_y^2 - c\phi_x\phi_y} \tag{11}$$

where ϕ is a three-dimensional function that evolves such that its zero level set tracks the evolving curve $\alpha(s)$, i.e.

$$\alpha(s, t) = \phi^{-1}(0). \tag{12}$$

The two geodesic distance maps D_S and D_D can now be defined by solving the propagation Eq. (11) on a graph surface Z twice, once for S and once for D, such that $D_S = \phi(x, y)$ and $D_D = \psi(x, y)$. The signed Euclidian distance maps ϕ_0 and ψ_0 of the curves S and D, respectively, are used as initial estimates [4]. The graph surface Z on which these geodesic distance maps are computed has to be the same for the computation of both maps in order to define a similarity measure between S and D. Z should also have both S and D as zero level sets. One such surface is

$$Z(x, y, z(x, y)) = \min(|\phi_0|, |\psi_0|) \tag{13}$$

Modifications to the graph surface can be incorporated, for example, to allow for geometrical properties of the curves to be taken into account. This is helpful when geometric similarities exist between the matched curves, however, there is a limited range over which the geometrical similarity is considered [8].

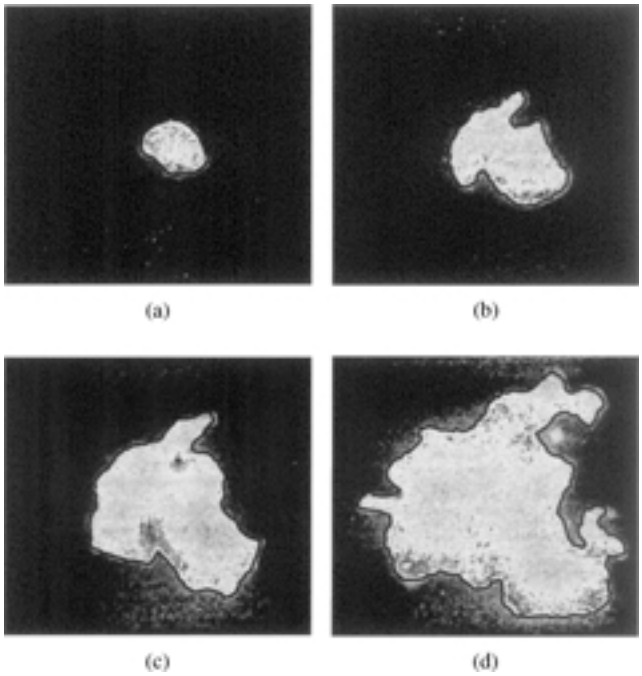

Figure 7. Segmenting the images of Fig. 4 using ACM. The results are overlaid on the original images of Fig. 2.

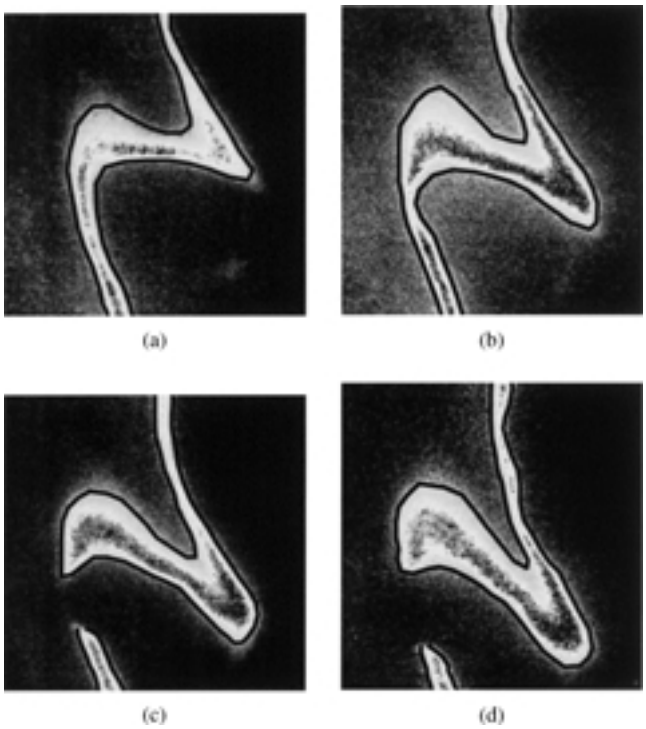

Figure 8. Segmenting the images of Fig. 5 using active contour models. The results are overlaid on the original images of Fig. 3.

Since the minimal paths are orthogonal to the equal distance contours, they can be reconstructed by starting on a point on the source contour and moving in the direction of the gradient of the cost function until reaching the destination curve. The path is thus defined by a parameterized curve $p(s)$ such that

$$\frac{\partial p}{\partial s} = -\nabla f(x, y). \tag{14}$$

In our implementation, the gradient of the cost function is smoothed using a 2D-Gaussian kernel, which gives more plausible and robust results.

4.3. Matching with Point Correspondence

To improve the quality and stability of the matching results when geometrically similar feature points on the curves have moved over a wide range, we propose adding an additional term, D_C, to the cost function $f(x, y)$. This term steers the algorithm into matching certain distinctive landmarks when their correspondence can be accurately identified.

We define D_C as

$$D_C(x, y) = \sum_{i=1}^{N} w_i(x, y)\big(D_{p_{i1}}(x, y) - D_{p_{i2}}(x, y)\big) \tag{15}$$

where $\langle p_{i1}, p_{i2}\rangle = \langle (x_{i1}, y_{i1}), (x_{i2}, y_{i2})\rangle$ is the i^{th} pair of landmark points to be matched and $D_{p_{i1}}$ and $D_{p_{i2}}$ are their Euclidean distance maps. N is the number of pairs used. $w_i(x, y)$ is a weighting factor incorporated in order to localize the effect of the matching term, i.e. to attenuate its effect as the distance to $\langle p_{i1}, p_{i2}\rangle$ increases and is defined as

$$w_i(x, y) = \alpha\big(d_{p_{i1}}(x, y) + d_{p_{i2}}(x, y)\big)^{-\beta} \tag{16}$$

where α and β are positive constants, and $d_{p_{ij}}(x, y) = \sqrt{(x - x_{ij})^2 + (y - y_{ij})^2}$, $j = 1, 2$. The values used here are $\alpha = 2.5$ and $\beta = 0.4$.

D_C can be viewed as adding new components to the cost function that act as a field steering corresponding landmark pairs to each other, see Fig. 9. Accordingly, the cost function becomes

$$f(x, y) = D_S + D_D + D_C. \tag{17}$$

The pairs of points to be matched can be identified either manually or automatically. Here an automatic algorithm for critical point detection (CPD) on a simple closed 2-D object boundary is used [31]. This CPD algorithm does not require curvature estimation or Gaussian filtering, instead, a set of candidate points called pseudo critical points (denoted C_o) is initially generated from the original boundary curve. This is done by first transforming the curve points to polar coordinates thus obtaining two one dimensional curves, $\rho(s)$ and $\theta(s)$. C_o is then defined to be the set of points where ρ and θ have local minima or maxima. Assigned to each point in C_o is a critical level defined by the

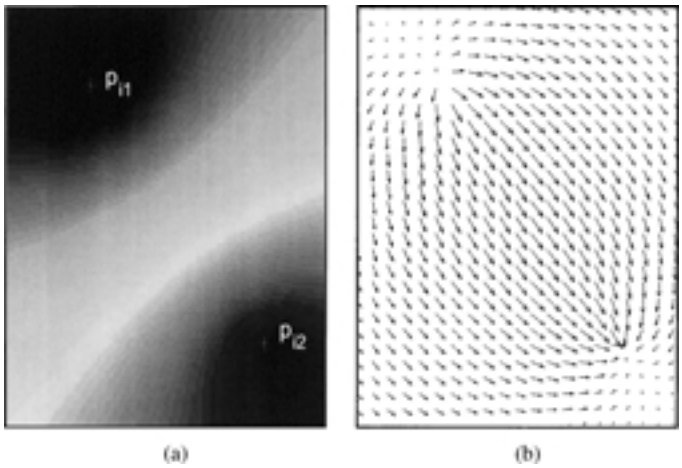

Figure 9. Matching a pair of corresponding points. (a) The additional cost term D_C in the vicinity of $\langle p_{i1}, p_{i2}\rangle$. (b) The gradient ∇D_C, which acts as a field steering p_{i1} to p_{i2}.

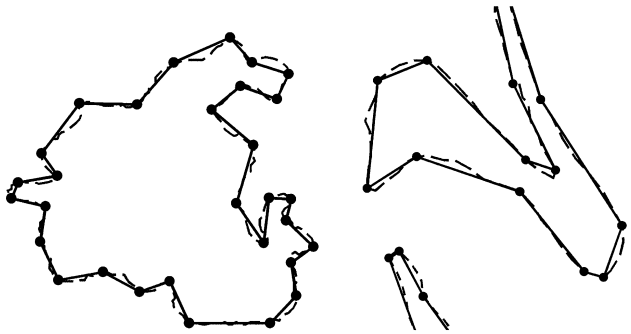

Figure 10. CPD applied to flame boundary contours of (a) Fig. 7(d) and (b) Fig. 8(c). Original curves (dashed) and the critical points (connected dots).

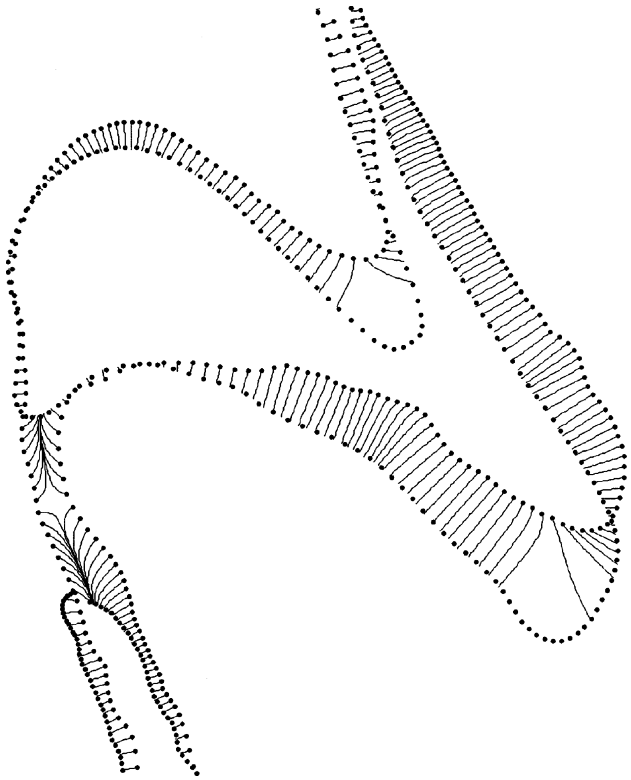

Figure 11. Matching paths of flame contours extracted from the two frames (b and c) in the diffusion flame sequence shown in Fig. 3 *without* incorporating point correspondence.

area of the triangle formed by that point and its two pseudo critical neighbors. The points with the lowest critical level are then deleted recursively until only the "true" critical points remain, i.e. those with critical levels higher than a specified level. An example illustrating this is shown in Fig. 10.

An example illustrating the matching paths *without* incorporating point correspondence is shown in Fig. 11.

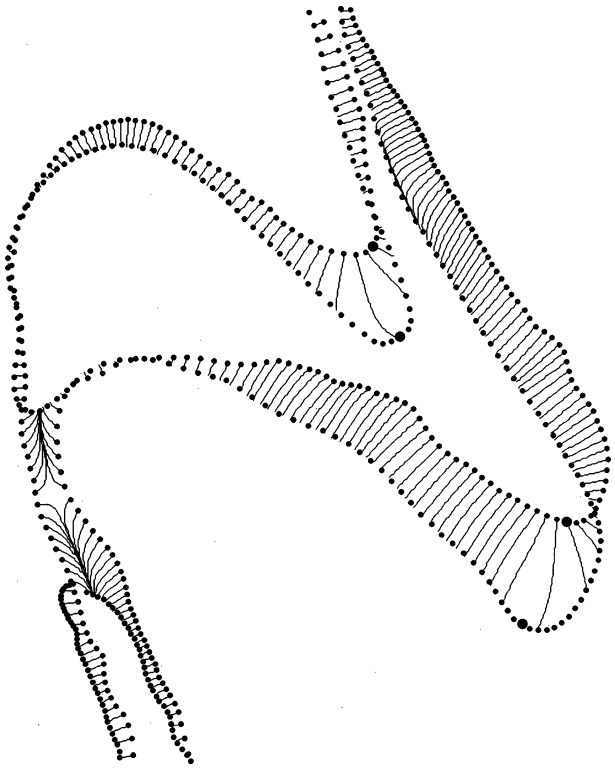

Figure 12. Improving the matching results shown in Fig. 11 by incorporating two pairs of corresponding points (marked as black dots).

Figure 12 illustrates the improvements of the matching results when the proposed point correspondence term D_C is incorporated within the matching cost function.

5. Velocity Measurements

At this point, it is possible to extract the flame front and the flow field velocities for conducting quantitative comparisons.

5.1. Flame Front Velocity

As matching paths between consecutive flame front contours in OH-PLIF image sequences are traced, flame motion can be reconstructed between experimentally captured frames and flame front velocities can be estimated. Assuming constant contour node velocity between a pair of consecutive frames, velocities are obtained by dividing the distance traveled by each node of the flame contour by the time it takes to move that distance (which is the original inter-frame interval applied while conducting the experiments). Figure 13 shows the calculated flame front velocities for the sequence shown in Fig. 3 where the velocity values are illustrated as a color-coded map.

5.2. Flow Field

PIV methods have developed rapidly over the past years as recording and evaluation techniques moved from analog to digital platforms. Fast digital cameras have replaced the initial analog methods that use photographic films and optical correlation methods. In PIV the velocity is calculated from the measured displacement of fluid elements in a known time. In order to accomplish this, the flow is seeded with small particles ($\sim\mu$m TiO_2 particles in our case) that trace the motion of the fluid. A pulsed laser is used to obtain images of the seed particles by firing it twice with a suitable time interval in between. This way, two images are acquired with a CCD camera (as described earlier), which are then processed to find the velocity vector map of the flow field.

The processing starts by first dividing the two images, Im_1 and Im_2, into small areas called interrogation

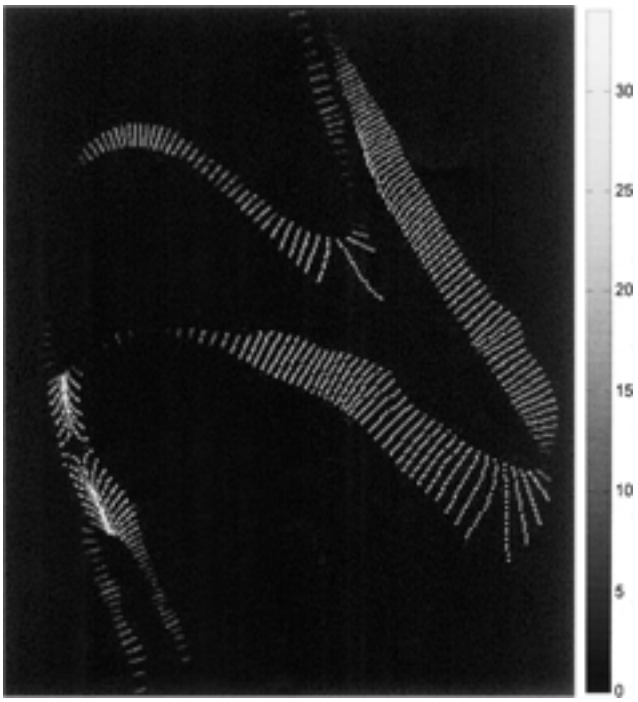

Figure 13. Flame front velocities estimated from the OH-PLIF image sequence shown in Fig. 8 (frames b and c). The color-bar to the right shows the velocity values in m/s.

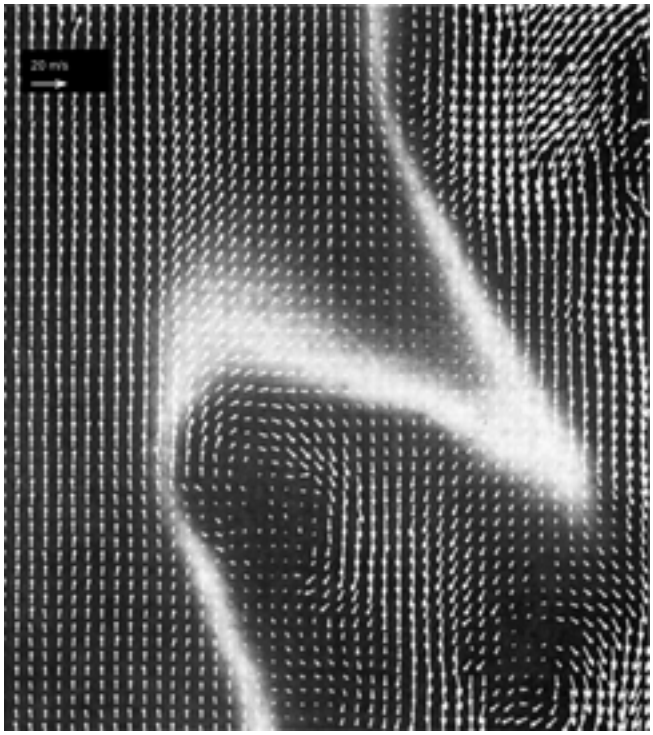

Figure 14. Flow field vector map estimated from the PIV image data corresponding to the sequence of Fig. 3 after mean subtraction of a 9 m/s vertical velocity for better visualization. The scale is shown to the upper left.

regions, then the displacement of groups of particles within each interrogation region is measured using a correlation technique. The cross correlation function determines the match between local regions at different time steps and is discretely defined by

$$R(x, y) = \sum_{i=-M/2}^{M/2} \sum_{j=-N/2}^{N/2} Im_1(i, j) Im_2(i + x, j + y) \tag{18}$$

where M and N determine the size of the interrogation region and are usually equal. The positions of the peaks in R are then used to determine the displacements. From these displacements the velocity vectors are calculated in each region and the complete 2D velocity vector map is determined.

Full details of the methods used for the PIV measurements are reported in [16]. Briefly, the PIV images were divided into interrogation areas of 32×32 pixels corresponding to volumes of $0.7 \times 0.7 \times 0.4$ mm^3. 62×62 velocity vectors were produced with a 50% overlap between regions giving a spatial vector resolution of 0.35 mm. The instantaneous vector maps were processed using a 4 step validation chain, described in detail in [16], which removed erroneous vectors. The subject of PIV measurements and issues specifically related to measurements in combusting systems can be found in [24]. For a comparison of different velocity mapping processing techniques see [23].

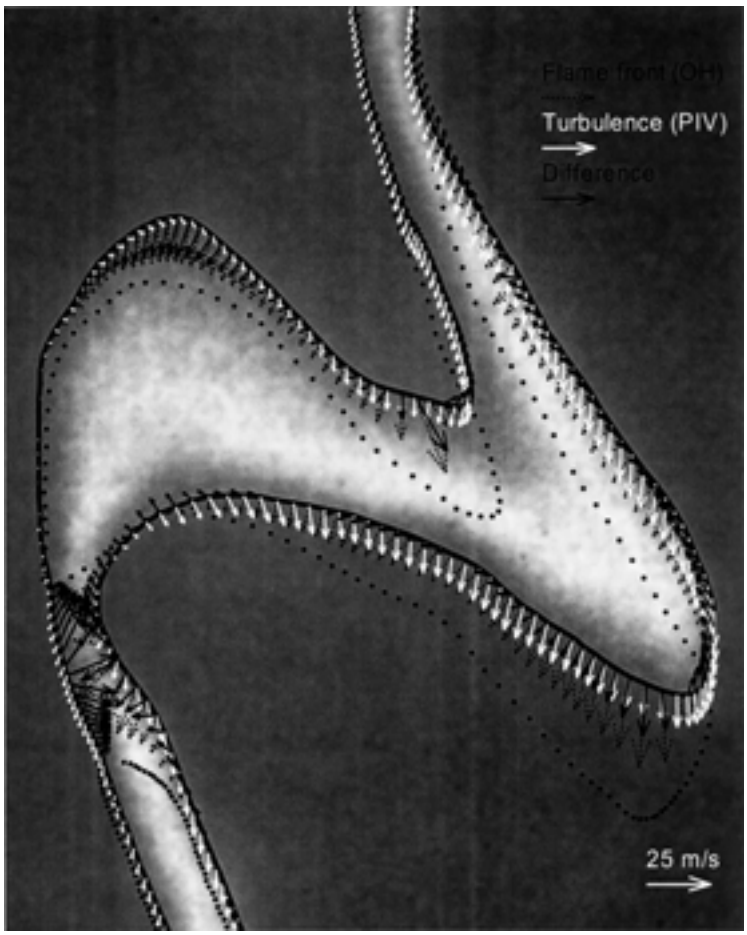

Figure 15. OH-PLIF vs. PIV velocity vector comparisons at the flame front. The thick black curve is the source and the dotted curve is the destination. The white arrows are the flow field vectors, the dotted arrows are the flame front velocity vectors, and the solid black arrows are the difference vectors. The scale is shown to the lower right.

Finally, the OH images are remapped to the coordinate system of the PIV images and the velocity vectors are plotted on top of the corresponding OH image. An example of the resulting velocity vectors for the sequence shown in Fig. 3 is shown in Fig. 14.

6. Results

Now that both the two-dimensional flow field (from the PIV images) and the flame front velocities (from the OH-PLIF images) are separately measured, it is possible *for the first time* to make direct comparisons between the two. Turbulence can greatly enhance the rate at which chemical species proceed to react by increasing the mixing rates of reactants. However excessive strain on the flame front, caused by turbulent convection can also have the opposite effect: The flame front thins, and radiative losses can lead to flame extinction. The event witnessed in the sequence shown in Fig. 3 is precisely of that nature. Although it is clear that flame extinction is taking place in this sequence, it is interesting to compare the physical mechanisms leading to this event in more detail. The presented techniques allow a more precise interpretation of the physics behind turbulent flame extinction than has been possible before. Figure 12 clearly shows how the flame front is moving as the extinction process is taking place. The source curve shows a connected flame front that is heavily stretched. This can be observed from the solid lines that show the estimated trajectories of points within the flame front as it proceeds through the extinction event towards the topologically altered destination curve. This stretching thins the flame front at a rapid rate as can be seen from the color-coded map in Fig. 13 (white: highest velocity). Since the flame front velocity values reflect the global flame motion, which is a consequence of both

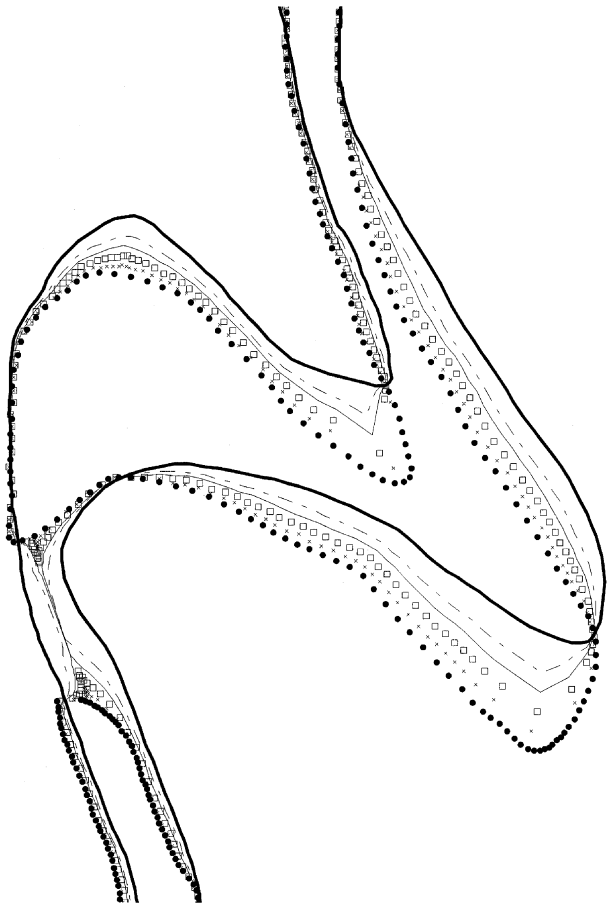

Figure 16. Visualization of intermediate frames within the experimentally captured image sequence of Fig. 3 (between frames b and c).

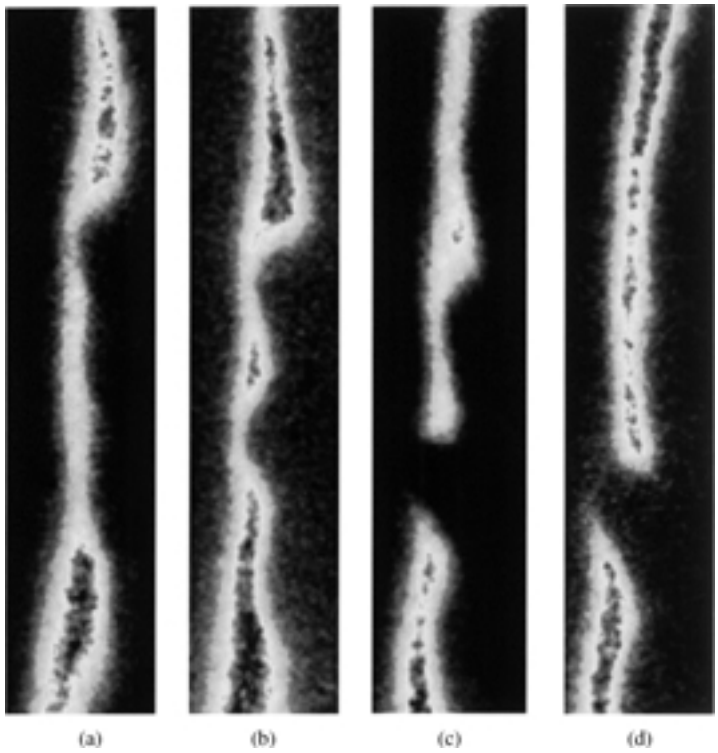

Figure 17. Another example of diffusion flame sequences. (a)–(d) Four frames captured with 75 microsecond interframe interval.

turbulent convection and chemical reactions, one way to compare the results is to subtract the fluid flow velocity (obtained from PIV) from the local flame front velocity (obtained by the geodesic path analysis). The results are shown in Fig. 15. Frame interpolations are shown in Fig. 16. The directional variations between the flame front velocity vectors and the difference vectors (i.e. the flame front velocities from which the fluid flow is subtracted) give an indication of the effect of convection on the flame front. Near the region of the extinction event, the two sides of the 'OH braid' are rapidly approaching each other, leading to the flame front thinning effect discussed. In this region the fluid flow and the flame front movement are carrying combustible mixture into an ever more thinning region. The opposite effect is observable in the region above the extinction event, in the upper left quadrant of image. Such effects can only be visualized with the current approach.

Our proposed algorithms were tested on a number of different image sequences. Figure 17 shows another example illustrating a diffusion flame sequence. The four frames, captured with 75 microsecond interframe interval, depict an extinction event of a thinning flame.

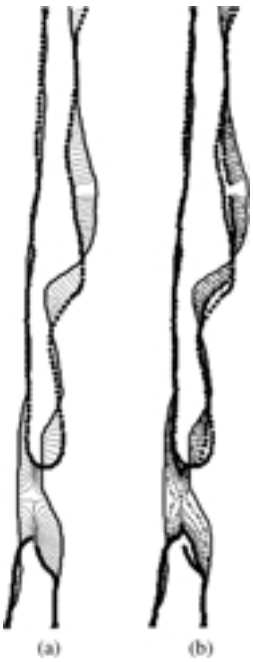

Figure 18. Curve matching of flame fronts extracted from Fig. 17(b) and (c). (a) Matching paths. (b) Interpolated curves (gray colors) between the original flame fronts (black).

Figure 18 illustrates the curve matching process of the flame fronts extracted from Fig. 17 (b) and (c). Figure 18(a) shows the matching paths obtained using our proposed technique while Fig. 18(b) shows the resulting interpolated curves (drawn in gray colors) between the original flame fronts (drawn in black).

Figure 19(a) presents the resulting flame front velocities estimated from the OH-PLIF image sequence. In Fig. 19(b) we show the flow field vector map estimated from the PIV images after the subtraction of a 24 m/s mean vertical velocity for better visualization. Figure 20 illustrates the obtained measurements of the flame front velocity vectors, the PIV vectors, and the difference vectors for the sequence.

7. Discussion and Conclusion

We show how OH-PLIF images of combustion flames can be analyzed to study the effects of turbulent flow fields on the reaction zone structure. We present image analysis techniques suitable for studying real time temporal image data sequences obtained by a combination of two measurement techniques for the purpose of decoupling chemistry interaction effects from turbulence effects in diffusion (non-premixed) flames. The capability of tracking flame contours in time as shown here, for the first time, facilitates the study of flame dynamics. For instance, once the contours are matched, the matching paths can be used to visualize intermediate frames within the experimentally sampled image

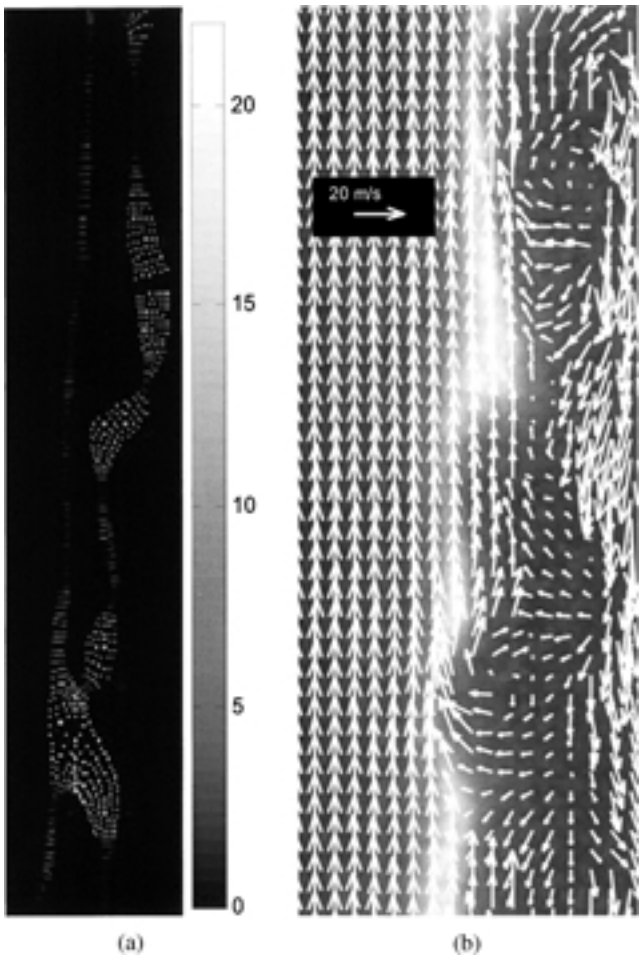

Figure 19. (a) Flame front velocities estimated from the OH PLIF image sequence. The color bar to the right shows the velocity values in m/s. (b) Flow field vector map estimated from the PIV image after the subtraction of a 24 m/s mean vertical velocity for better visualization. The scale is shown to the upper left.

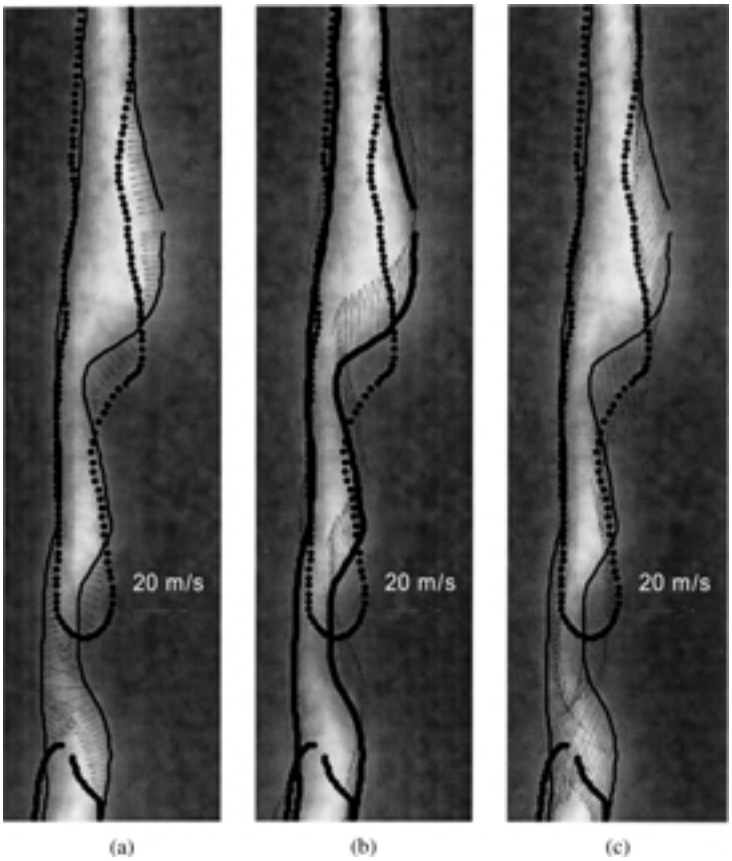

Figure 20. Velocity measurements for the sequence of Fig. 17. The white arrows show the scale. (a) Flame front velocity vectors. (b) PIV vectors. (c) Difference vectors.

sequences (as shown in Fig. 16) and flame front velocities can be estimated. The curve matching methods presented here provide alternative methods to study the movement of flame fronts subjected to turbulent flow fields. This can be used for model development and validation of technical combustion processes. In combination with standard flow velocimetry techniques such as particle imaging velocimetry (PIV), the present technique provides a unique way to track the response of the flame front in the presence of turbulence. Applications range from aero and automobile engine research to the design of technical combustors used in industry and for heating.

Although the presented techniques provide extensive information on flow and chemistry interactions, it must be remembered that they are confined to a single measurement plane and thus cannot give consideration to three-dimensional effects such as vortex motion in and out of the measurement planes. Three-dimensional measurement approaches (for example PLIF coupled with stereo-PIV techniques) could yield further information in this respect.

Acknowledgments

The authors would like to acknowledge Dr. Johan Hult for the provision of OH and PIV data, for provision of Fig. 1, and for useful discussions throughout the project.

References

1. R. Abu-Gharbieh, G. Hamarneh, T. Gustavsson, and C. Kaminski, "Flame front tracking by laser induced fluorescence spectroscopy and advanced image analysis," *Journal of Optics Express*, Vol. 8, No. 5, pp. 278–287, 2001.

2. R. Abu-Gharbieh, G. Hamarneh, and C. Kaminski, "Flame front matching and tracking in PLIF images using geodesic paths and level sets," in *Proceedings of the IEEE Workshop on Variational and Level Set Methods in Computer Vision*, Vancouver, July 2001.
3. B.M. Atakan, V. Jörres, and K.K. Höinghaus, "Double pulse 2D LIF as a means for following flow and chemistry development in turbulent combustion," *Ber. Bunsenges. Phys. Chem.*, Vol. 97, pp. 1706–1710, 1993.
4. G. Borgefors, "Distance transformations in arbitrary dimensions," *Journal of Computer Vision, Graphics, and Image Processing*, Vol. 27, pp. 321–345, 1984.
5. A. Brockhinke, K. Kohse-Höinghaus, and P. Andresen, "Double pulse one-dimensional Raman and Rayleigh measurements for the detection of temporal and spatial structures in a turbulent H_2-air diffusion flame," *Optics Letters*, Vol. 21, pp. 2029–2031, 1996.
6. F. Catté, P.-L. Lions, J.-M. Morel, and T. Coll, "Image selective smoothing and edge detection by nonlinear diffusion," *SIAM Journal on Numerical Analysis*, Vol. 29, pp. 182–193, 1992.
7. Y.-C. Chen and M.S. Mansour, "Topology of turbulent premixed flame fronts resolved by simultaneous planar imaging of LIPF of OH radical and Rayleigh scattering," *Experiments in Fluids*, Vol. 26, pp. 277–287, 1999.
8. I. Cohen and I. Herlin, "Curves matching using geodesic paths," *IEEE Conference on Computer Vision and Pattern Recognition*, pp. 741–746, 1998.
9. I. Cohen and I. Herlin, "Tracking meteorological structures through curves matching using geodesic paths," in *Proceedings of the International Conference on Computer Vision*, 1998, pp. 396–401.
10. T. Ding, Th. Van Der Meer, M. Versluis, M. Golombok, J. Hult, M. Aldén, and C.F. Kaminski, "Time-resolved PLIF imaging in turbulent diffusion flames," in *Proceedings of the International Symposium on Turbulence, Heat, and Mass Transfer, Nagoya*, 2000, pp. 857–864.
11. A. Dreizler, S. Lindenmaier, U. Maas, J. Hult, M. Aldén, and C.F. Kaminski, "Characterization of a spark ignition system by planar-laser-induced fluorescence of OH at high repetition rates and comparisons with chemical kinetics calculations," *Applied Physics B*, Vol. 70, pp. 287–294, 2000.
12. M.J. Dyer and D.R. Crosley, "Rapidly sequenced pair of two-dimensional images of OH by laser induced fluorescence in a flame," *Optics Letters*, Vol. 9, pp. 217–219, 1984.
13. J.H. Frank, K.M. Lyons, and M.B. Long, "Simultaneous scalar/velocity measurements in turbulent gas-phase flows," *Combustion and Flame*, Vol. 107, pp. 1–12, 1996.
14. O.L. Gulder, G.J. Smallwood, R. Wong, D.R. Snelling, R. Smith, B.M. Deschamps, and J.-C. Sautet, "Flame front surface characteristics in turbulent premixed propane/air combustion," *Combustion and Flame*, Vol. 120, No. 4, pp. 407–416, 2000.
15. B.D. Haslam and P.D. Ronney, "Fractal properties of propagating fronts in a strongly stirred fluid," *Physics of Fluids*, Vol. 7, No. 8, pp. 1931–1937, 1995.
16. J. Hult, G. Josefsson, M. Aldén, and C.F. Kaminski, "Flame front tracking and simultaneous flow field visualization in turbulent combustion," in *Proceedings of the International Symposium on Applications of Laser Techniques to Fluid Mechanics*, Lisbon, 2000.
17. C.F. Kaminski, J. Hult, and M. Aldén, "High repetition rate planar laser induced fluorescence of OH in a turbulent non-premixed flame," *Applied Physics B*, Vol. 68, pp. 757–760, 2000.
18. M. Kass, A. Witkin, and D. Terzopoulos, "Snakes: Active contour models," *International Journal on Computer Vision*, Vol. 1, No. 4, pp. 321–331, 1988.
19. R. Kimmel, A. Amir, and A. Bruckstein, "Finding shortest paths on surfaces using level sets propagation," *IEEE Transactions on Pattern Analysis and Machine Intelligence*, Vol. 17, No. 6, pp. 635–640, 1995.
20. R. Knikker, D. Veynante, J.C. Rolon, and C. Meneveau, "Planar laser-induced fluorescence in a turbulent premixed flame to analyze large Eddy simulation models," in *Proceedings of the International Symposium on Turbulence, Heat and Mass Transfer*, Lisbon, 2000.
21. G. Kychakoff, P.H. Paul, I.V. Cruyningen, and R.K. Hanson, "Movies and 3D images of flow fields using planar laser-induced fluorescence," *Applied Optics*, Vol. 26, pp. 2498–2500, 1987.
22. H. Malm, J. Hult, G. Sparr, and C.F. Kaminski, "Non-linear diffusion filtering of images obtained by planar laser induced florescence spectroscopy," *Journal of the Optical Society of America A (JOSA A)*, Vol. 17, No. 12, pp. 2148–2156, 2000.
23. S.P. McKenna and W.R. McGillis, "Performance of digital image velocimetry processing techniques," *Experiments in Fluids*, Vol. 32, pp. 106–115, 2002.
24. R.B. Miles, "Flow field diagnostics," in *Applied Combustion Diagnostics*, K.K. Hoinghaus and J.B. Jeffries (Eds.), Taylor and Francis, 2002, ch. 7.
25. P. Perona and J. Malik, "Scale-space and edge detection using anisotropic diffusion," *IEEE Transactions on Pattern Analysis and Machine Intelligence*, Vol. 12, No. 7, pp. 629–639, 1990.
26. M.W. Renfro, W.A. Guttenfelder, G.B. King, and N.M. Laurendeau, "Scalar time series measurements in turbulent $CH_4/H_2/N_2$ nonpremixed flames: OH," *Combustion and Flame*, Vol. 123, pp. 389–401, 2000.
27. G.J. Smallwood, O.L. Gulder, D.R. Snelling, B.M. Deschamps, and I. Gokalp, "Characterization of flame front surfaces in turbulent premixed methane/air combustion," *Combustion and Flame*, Vol. 101, No. 4, pp. 461–470, 1995.
28. K.A. Watson, K.M. Lyons, J.M. Donbar, and C.D. Carter, "Scalar and velocity field measurements in a lifted CH_4—Air diffusion flame," *Combustion and Flame*, Vol. 117, pp. 257–271, 1999.
29. J. Weickert, *Anisotropic Diffusion in Image Processing*, Stuttgart: ECMI Series, Teubner, 1998.
30. M. Winter and M.B. Long, "Two dimensional measurements of the time development of a turbulent premixed flame," *Combustion Science and Technology*, Vol. 66, pp. 181–188, 1989.
31. P. Zhu and P.M. Chirlian, "On critical point detection of digital shapes," *IEEE Transactions on Pattern Analysis and Machine Intelligence*, Vol. 17, No. 8, pp. 737–748, 1995.

Rafeef Abu-Gharbieh received her B.Sc. in Electrical Engineering from the University of Jordan in Amman, Jordan in 1995 and her Honors M.Sc., Technical Licentiate, and Ph.D. degrees in Electrical and Computer Engineering from Chalmers University of Technology in Goteborg, Sweden, in 1996, 1999 and 2001 respectively. Her Ph.D. thesis focused on laser sheet imaging and image analysis for combustion research. She is Currently an Assistant Professor at Ryerson University in Toronto, Canada.

Abu-Gharbieh's research interests are in the field of image processing and analysis and its applications including medical image computing and laser image diagnostics.

Ghassan Hamarneh received his Ph.D., Technical Licentiate, Honors M.Sc. from the School of Electrical and Computer Engineering, Chalmers University in Goteborg, Sweden, and his B.Sc. in Electrical Engineering from the University of Jordan in Amman, Jordan, in 2001, 1999, 1997, and 1995, respectively. His Ph.D. thesis focused on the development and application of intelligent deformable models for medical image analysis. During 2000–2001, Hamarneh was a predoctoral scholar at the Vision and Visual Modeling Group at the University of Toronto and is currently a postdoctoral fellow at the Mouse Imaging Centre, Hospital for Sick Children in Toronto, Canada. Hamarneh's general research interests include image processing, medical image analysis, image segmentation, registration, and visualization, physics-based shape modeling, and statistical analysis of shape deformations.

Tomas Gustavsson was born on January 6 in 1954. He received the M.Sc. and Ph.D. degrees in Electrical and Computer Engineering from Chalmers University of Technology, Gteborg, Sweden, in 1983 and 1991, respectively. He is currently a Professor in the Department of Signals and Systems, Chalmers. Gustavsson is active in the field of medical image analysis. Current research includes development of bioimaging systems (light-, electron-, fluorescence-, and time-lapse microscopy) and physics based modeling with applications to cardiovascular, neuro and cellular imaging. Examples are deformable modeling for boundary detection in ultrasonic heart images, mathematical-statistical modeling for stem cell motion tracking, and statistical classification of medical color images.

Clemens Kaminski is a university lecturer at the Chemical Engineering Department at the University of Cambridge, UK since 2001. He completed his Ph.D. in physics at Oxford University on the development of novel non-linear laser techniques for diagnostics of plasmas and flames. He joined the Division of Combustion Physics in Lund, Sweden, in 1995 where he was appointed as an associate professor in engineering physics. His research interests center around the development of novel laser based imaging tools to visualise chemical phenomena both in microscopic and in macroscopic systems and has published more than 30 peer reviewed papers. Current research projects span a range of applications from tracking pollutants and their formation in next generation low emission gasturbine concepts, down to tracking individual molecules in living cells for drug discovery research. He colloborates heavily with industry and is a member of the Optical Society of America, the Combustion Institute and serves as programme chair of the 2004 international conference on Laser Applications in Chemical and Environmental Analysis (LACEA 2004) to be held in Annapolis, USA.